THE JOURNAL OF BIOLOGICAL CHEMISTRY VOL. 285, NO. 30, pp. 23351–23358, July 23, 2010
Printed in the U.S.A.

Multiple Modes of Endophilin-mediated Conversion of Lipid Vesicles into Coated Tubes

IMPLICATIONS FOR SYNAPTIC ENDOCYTOSIS[*] [S]

Received for publication, May 11, 2010 Published, JBC Papers in Press, May 18, 2010, DOI 10.1074/jbc.M110.143776

Naoko Mizuno[‡], **Christine C. Jao**[§], **Ralf Langen**[§], **and Alasdair C. Steven**[‡1]

From the [‡]*Laboratory of Structural Biology, National Institute of Arthritis and Musculoskeletal and Skin Diseases, National Institutes of Health, Bethesda, Maryland 20892 and the* [§]*Zilkha Neurogenetic Institute, University of Southern California, Los Angeles, California 90033*

Endophilin A1 is a BAR (Bin/amphiphysin/Rvs) protein abundant in neural synapses that senses and induces membrane curvature, contributing to neck formation in presynaptic endocytic vesicles. To investigate its role in membrane remodeling, we used cryoelectron microscopy to characterize structural changes induced in lipid vesicles by exposure to endophilin. The vesicles convert rapidly to coated tubules whose morphology reflects the local concentration of endophilin. Their diameters and curvature resemble those of synaptic vesicles *in situ*. Three-dimensional reconstructions of quasicylindrical tubes revealed arrays of BAR dimers, flanked by densities that we equate with amphipathic helices whose folding and membrane insertion were attested by EPR. We also observed the compression of bulbous coated tubes into 70-Å-wide cylindrical micelles, which appear to mimic the penultimate (hemi-fission) stage of endocytosis. Our findings suggest that the adaptability of endophilin-lipid interactions underlies dynamic changes of endocytic membranes.

At a synapse, where nerve cells communicate, neurotransmitters are released by exocytosis of synaptic vesicles. The vesicles are stored at nerve terminals, ready for rapid multiple secretions (up to 500 times per second) (1). To be able to process frequent neuronal signals, it is crucial that the carrier vesicles are rapidly retrieved from the membrane (2). Nerve cells employ a specialized set of synaptic components to conduct this recycling process.

BAR domain-containing proteins play important roles in synaptic endocytosis (3). They trigger and facilitate the deformation and tubulation of membranes (4). BAR proteins have crescent shapes whose curvature reflects the mode of dimerization of rod-like monomers (see Fig. 1*a*) (5–12). The BAR superfamily is subcategorized into three classes: I-BAR, F-BAR, and N-BAR (13). N-BAR domains recognize membranes with sharp positive curvature, F-BARs cover a range of less extreme positive curvatures (14), and I-BARs recognize negative curvatures (15, 16). Furthermore, N-BAR domains have an N-terminal amphipathic helix that inserts into membranes and is thought to be crucial for membrane bending (7, 17). Interactions of BAR proteins with membranes have been studied, structurally and computationally (17–19). Electron microscopy (EM)[2] observations (5, 6, 20) have shown BAR-induced tubulation of vesicles. Tube diameter appears to depend on the concave curvature of the specific BAR domains. For instance, F-BAR proteins, which induce much wider tubes, have more open crescent shapes than N-BARs. Tubulated vesicles coated with regular arrays of BAR proteins have been observed by cryo-EM (10, 20). Molecular dynamic simulations have predicted that different packing arrangements of the N-BAR protein amphiphysin on flat membranes can lead to various sizes of tubes (21). However, it has not been clear how the actual tubulation process occurs.

Endophilin A1 is an N-BAR protein (22–26) with a C-terminal SH3 domain (see Fig. 1*a*, *right*) (27). The BAR domain structure has been determined, revealing a positively charged concave surface that has been proposed to bind to membranes with radii of curvature in the range of ~85–140 Å (7, 12, 28). Moreover, analysis by EPR spectroscopy has shown that both the N-terminal amphipathic helix (H0), presumably located at the ends of the dimer, and the centrally placed helix 1 insert region (H1I) interact with membranes (7, 49) (see Fig. 1*a*). These motifs were disordered in the crystal structures but fold upon encountering a membrane. H0 is important for membrane tubulation (7, 29, 30), but the role of H1I in this process is not yet clear. However, deletion of H1I is known to abolish dimer formation, and it has been suggested to form a helix that acts as a wedge upon contacting a membrane (7, 29).

To investigate the interactions of endophilin with membranes, we have conducted cryo-EM studies of endophilin A1 BAR domains mixed with preformed phospholipid vesicles. Image analysis and three-dimensional reconstruction were performed on the tubes produced. Strands of endophilin dimers associated tail-to-tail were observed coating tubular lipid bilayers, but also, unexpectedly, we observed very thin tubes that we infer to represent coated cylindrical micelles. Finally, we discuss the potential implications of these observations, in partic-

* This work was supported, in whole or in part, by the Intramural Research Program of NIAMS, National Institutes of Health and by National Institutes of Health Grant GM063915 (to R. L.).

[S] The on-line version of this article (available at http://www.jbc.org) contains supplemental Figs. 1–5 and Table.

[1] To whom correspondence should be addressed: Laboratory of Structural Biology Research, NIAMS, Bldg. 50, Rm. 1517, NIH, Bethesda, MD 20892-8025. Tel.: 301-496-0132; Fax: 301-443-7651; E-mail: stevena@mail.nih.gov.

[2] The abbreviations used are: EM, electron microscopy; POPG, [1-palmitoyl-2-oleoyl-SN-glycero-3-[phospho-RAC-(1-glycerol)]; IHRSR, iterative helical real space reconstruction.

ular, involving the versatility and flexibility of endophilin-membrane interactions, for dynamic processes *in vivo*.

EXPERIMENTAL PROCEDURES

Preparation of Endophilin A1 BAR Domain and Multilamellar Vesicles—Rat endophilin A1 BAR domain protein (residues 1–247) was prepared as described (7). Briefly, it was expressed as a glutathione *S*-transferase fusion protein, purified on glutathione beads, and followed by anion exchange (7). [1-palmitoyl-2-oleoyl-SN-glycero-3-[phospho-RAC-(1-glycerol)] (POPG) was obtained from Avanti Polar Lipids (Alabaster, AL). Lipids were dried with nitrogen and desiccated overnight. To prepare vesicles, lipids were resuspended in buffer and vortexed. All experiments were performed in buffer containing 20 mM Hepes, pH 7.4, and 100 mM NaCl. BAR domain dimers and lipids were mixed at molar ratios of 1:10, 1:20, and 1:40. Vesicle concentration was kept fixed at 400 μM, whereas the amount of protein added was varied accordingly. Samples were incubated for 1 or 10 min before taking samples for cryo-EM.

EPR Experiments—Purified proteins were incubated with 5× molar excess of methanethiosulfonate spin label ([1-oxyl-2,2,5,5-tetramethylpyrroline-3-methyl]-methane-thiosulfonate), and unreacted spin label was removed on a PD-10 column (GE Healthcare). Protein labeled at residues 15 (15R1) and 70 (70R1) a concentration of 20 μM was incubated with vesicles, at 1:10, 1:20, and 1:40 molar ratios. Spectra were collected at successive time points using a Bruker EMX spectrometer fitted with an HS resonator, operated at 4-milliwatt incident microwave power using a field modulation of 1.5 gauss (for soluble samples) or 3.0 gauss (for membrane-bound samples) and a scan width of 100 gauss.

Cryoelectron Microscopy—Samples were applied to glow-discharged Quantifoil grids (EMS), incubated for 1 min, then blotted and vitrified on a Vitrobot cryostation (FEI) and observed on a CM200-FEG electron microscope (FEI) operated at 120 kV. Micrographs were recorded on film at magnifications of ×66,000 or ×38,000 and defocus values ranging from 0.6 to 2.5 μM. A Zeiss SCAI scanner was used for digitization with 7 μm sampling, giving 0.962 Å and 1.84 Å/pixel, respectively.

Image Processing—Image analyses were carried out using Bsoft (44), EMAN (45), and SPIDER (46). Digitized images were corrected for contrast transfer function effects by phase-flipping. Segments were boxed out along tubes with 90% overlap. Type A tubes were segmented with a box size of 600 pixels, and Type B tubes were segmented with a box size of 200 pixels. The images used for reconstructions were binned 4 times to increase the calculation speed. After classification using SPIDER, two well populated classes of images of Type A tubes (n = 992 for the wider tube and n = 815 for the narrower tube) were selected for reconstruction by IHRSR (31), implemented in SPIDER. Initial helical symmetries were estimated by drawing possible lattices on cylindrical surfaces of the appropriate circumference, namely 747 Å for the wider and 628 Å for the narrower tube. For the wider tube, the principal layer line reflections were assessed as first order Bessel functions (n = 1), *i.e.* 1-start helix. IHRSR calculations tried a range of starting values for azimuthal rotation and axial rise per lattice step. There was a strong tendency for the rise to converge to ~ 9.2 Å,

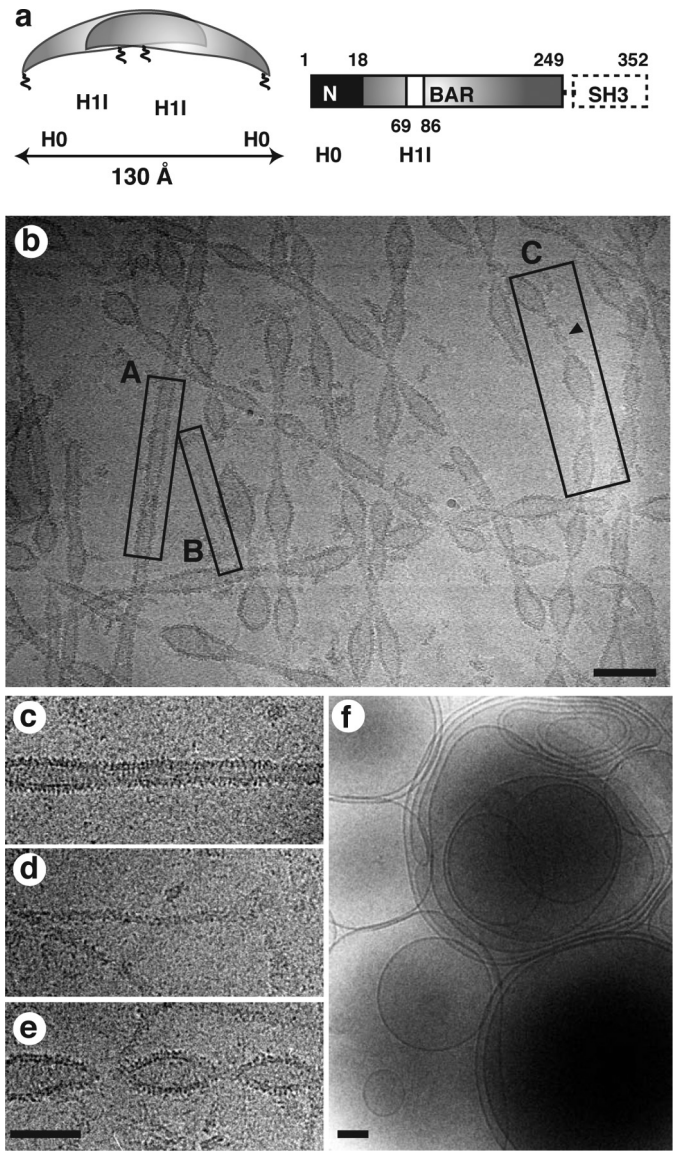

FIGURE 1. *a*, *schematic* of an endophilin BAR domain dimer (*left*) and the domain organization of the monomer (*right*). H0 and H1I are considered to form amphipathic helices in the presence of lipids (7). *b*, Cryoelectron micrograph of vesicle tubulation caused by endophilin. This experiment was performed at a molar ratio of 1:20 with a 10-min incubation prior to preparing the cryo-EM grid. Three morphologies were observed: Type A (*A*), relatively uniform tube; Type B (*B*), thin tubes (~70 Å); and Type C (*C*), tubes with bulbous protrusions. The *arrowhead* points to a Type C tube on which two bulbs are connected by a Type B-like segment. *Scale bar*, 500 Å. *c–e*, magnified images of Type A, B, and C tubes. *Scale bar*, 300 Å. *f*, cryo-EM micrograph of POPG vesicles without endophilin. *Scale bar*, 1000 Å.

but azimuthal rotation tended to converge locally. Reconstructions were calculated, and the correct solution was identified as the one that clearly gave the highest resolution, as measured by Fourier shell correlation. See supplemental Fig. 5 and Table. The solution gave a rotation angle of 68–70°, corresponding to a lattice step of ~130 Å. (*A priori*, this was a likely candidate because it matches the length of a BAR domain dimer.) Analyzed in essentially the same way, the thinner tube gave a four-start helix and a rotation angle of 74–76°. The resolution of the thinner tube was 15 Å according to the Fourier shell correction at a threshold of 0.3 (18 Å for threshold 0.5), and that of the wider tube 14 Å (or 21 Å) (supplemental Fig. 5). Unit cell areas

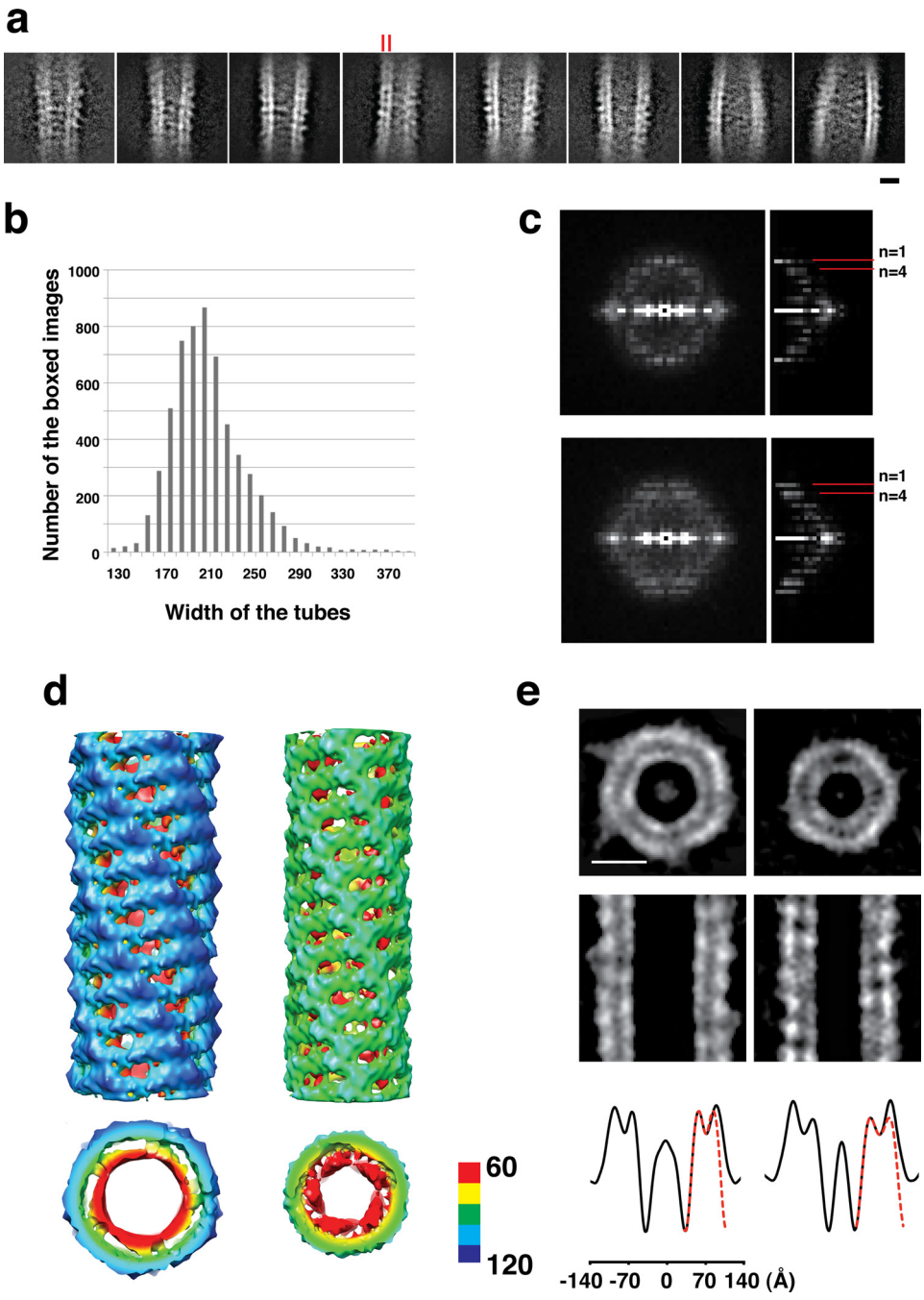

FIGURE 2. *a*, class average images of Type A tubes of differing width and straightness. *Red bars*, the two leaflets of the bilayer (one protein-coated) on an image in which they are well resolved. *Scale bar*, 100 Å. *b*, distribution of tube widths. *c*, averaged power spectra of image segments of the wider (*top left*) and narrower (*bottom left*) Type A tubes. Half-plane power spectra of reprojections of the corresponding reconstructions are shown on the *right*. *d*, three-dimensional reconstructions of the endophilin-coated tubes with diameters of 238 and 200 Å, respectively. The surface is color-coded according to the radius from the tube axis (see *colored scale*). The helical lattices are shown as right-handed on the assumption that they have the same hand as tubes of dynamin (48), a binding partner of endophilin. *e*, a transverse section (*left*), a longitudinal section (*middle*), and a scan of projected density along the longitudinal section (*right*) for the reconstructions shown in *d*. The *red dotted line* shows the mirrored inner leaflet for direct comparison with the outer leaflet. *Scale bar*, 100 Å.

were calculated to be 6190 Å^2 and 4374 Å^2 for the wider and narrower Type A tubes, respectively.

Docking of the Endophilin Crystal Structure—The endophilin BAR domain dimer (Protein Data Bank code 2c08) was docked manually into the cryo-EM reconstructions, using Chimera (47). Bsoft was used for low-pass filtering of the atomic models to give density maps and propogating them to follow the helical arrangement of the reconstruction.

RESULTS

Endophilin Variably Tubulates Membranes—When endophilin was added to preformed vesicles at molar ratios of 1:20 or 1:40 and observed shortly thereafter by cryo-EM, the large spherical vesicles originally present (Fig. 1*f*) were found to have been replaced by smaller curved and tubular membranes. Among them, we distinguish three morphologies, examples of which are labeled A, B, and C in the boxed areas of Fig. 1*b*. Type A tubes (Fig. 1*c*) are fairly uniform in width and are often seen protruding from round vesicles. Along both edges of the imaged tubes are two lines of density, corresponding to the inner and outer leaflets of the lipid bilayer. The outer line is serrated at a regular spacing of ~50 Å, indicative of a protein coating. The width of these tubes is typically ~240 Å but is somewhat variable, even along the same tube. Type B tubes (Fig. 1*d*) are very thin, with a width of only ~70 Å. On Type C tubes (Fig. 1*e*), a succession of bulbous protuberances are linked by narrow connections resembling Type B tubes (Fig. 1*b*, *arrowhead*); thus, their width oscillates between a maximum of ~350 Å and a minimum of ~70Å. We also visualized these specimens in three dimensions by cryo-electron tomography, and thus confirmed that the structures observed were indeed tubular and not ribbon-like (data not shown).

Molecular Architecture of Type A Tubes—To assess the packing of endophilin molecules on Type A tubes, these images were analyzed further. As the tubes vary somewhat in width along their lengths and from tube to tube, this analysis was conducted on a set of short (577 Å) and relatively uniform segments. These data were classified by correspondence analysis. Class average images are shown in Fig. 2*a* in inverted contrast relative to Fig. 1. They depict tube segments of various widths, ranging from 150 to 300 Å (Fig. 2*b*). Along most edges, the smooth line of density that

represents primarily the projection of the inner leaflet of the bilayer is well resolved from the jagged, endophilin-coated outer leaflet. (An example is indexed with two red lines in Fig. 2*a*.) The peripheral serrations are even more pronounced than in the original images.

The regularity of the edge serrations suggested that the endophilin molecules were packed in ordered arrays. To investigate this further, we calculated average diffraction patterns for the segments in two well populated classes, those with widths of ~200 and ~240 Å, respectively. The resulting diffraction patterns (Fig. 2*c*) show layer lines indicative of helical symmetry. The positions of the main reflections differ but are at about the same spacing, suggesting that the helical symmetries differ but are related. To determine the helical parameters of the wider tubes, we first noted that the equatorial coordinate of the main reflections (R), taken together with the radii of the peripheral striations (r) indicated that they correspond to a single-start helix ($2\pi Rr \sim 2$). To complete the determination, we used the iterative IHRSR approach (31), which, given a reasonable initial estimate of helical parameters, should converge to the correct solution. We tried a range of starting values and identified the optimal solution as that gave the highest resolution reconstruction. It is based on a single-start helix with 5.2 steps and 48 Å axial rise per turn. The analysis is described further under "Experimental Procedures." Analyzed in similar fashion, the narrower tubes were found to follow four-start helices with 6.0 lattice steps and 221 Å (55.3 Å × 4, see supplemental Fig. 2).

Both reconstructions show helically wound strands of elongated densities with an interstrand spacing of ~45 Å (Fig. 2*d*). The dimensions and shapes of these densities are consistent with endophilin dimers. On the wider tubes, their long axes are oriented at ~10° to the equator, and in the narrower tubes at ~25°, relative to the equator. Grayscale sections through the reconstructions (Fig. 2*e*) show that the outer leaflet, which is denser than the inner leaflet and, in the longitudinal sections, it is seen to be markedly more punctate, further confirming that the protein is coating a tubular lipid bilayer (Fig. 2*e*, *bottom*). In Fig. 2*d*, the reconstructions are color-coded according to radius relative to the tube axis. Referring back to the variable diameters of individual tubes, we surmise that this effect arises from interruptions in the regular patterns of interactions that give rise to the helical lattices.

Tail-to-tail and Lateral Interactions between Endophilin BAR Domain Dimers—Next, we sought to characterize the interdimer interactions further by fitting the crystal structure (Protein Data Bank code 2c08) into the reconstructions (Fig. 3, *a* and *e*). To minimize interference from lipid-associated density, the fitting was performed manually. The highest densities are located on the outer surface (supplemental Fig. 3, *a* and *d*), and the BAR domain dimer fits readily into this region (Fig. 3, *c* and *g* and supplemental Fig. 3, *a* and *c*). When the isodensity contour used for rendering is lowered, the outer leaflet starts to show up inside the endophilin densities (supplemental Fig. 3, *c* and *f*). The fitted endophilin crystal structure was propagated according to the helical symmetries of the two lattices, then low pass-filtered to 14 Å, to show the molecular packing more clearly (Fig. 3, *b* and *f*). As fitted, the surface area of the BAR domain dimer in contact with the lipid bilayer was calculated as ~5,000 Å^2 (40% of its total surface area) for the narrower tube and ~5,300 Å^2 (42.5%) for the wider tube. On the wider tubes, the dimers associate in tail-to-tail fashion (Fig. 3, *b–d*, *arrowhead*), as observed for other BAR domain proteins (20, 21). On the narrower tubes, there is some overlap, with the tail of one dimer contacting the side of a neighbor at a point ~38 Å from its tip (Fig. 3*h*, *arrowheads*). In the wider tubes, the dimer strands are almost equatorial (Fig. 3, *b* and *d*, $\psi = 7°$; see Fig. 3*i*), whereas in the narrower tubes, they are tilted at a pitch angle of ~23° (Fig. 3, *f* and *h*). The concave surface of the dimer

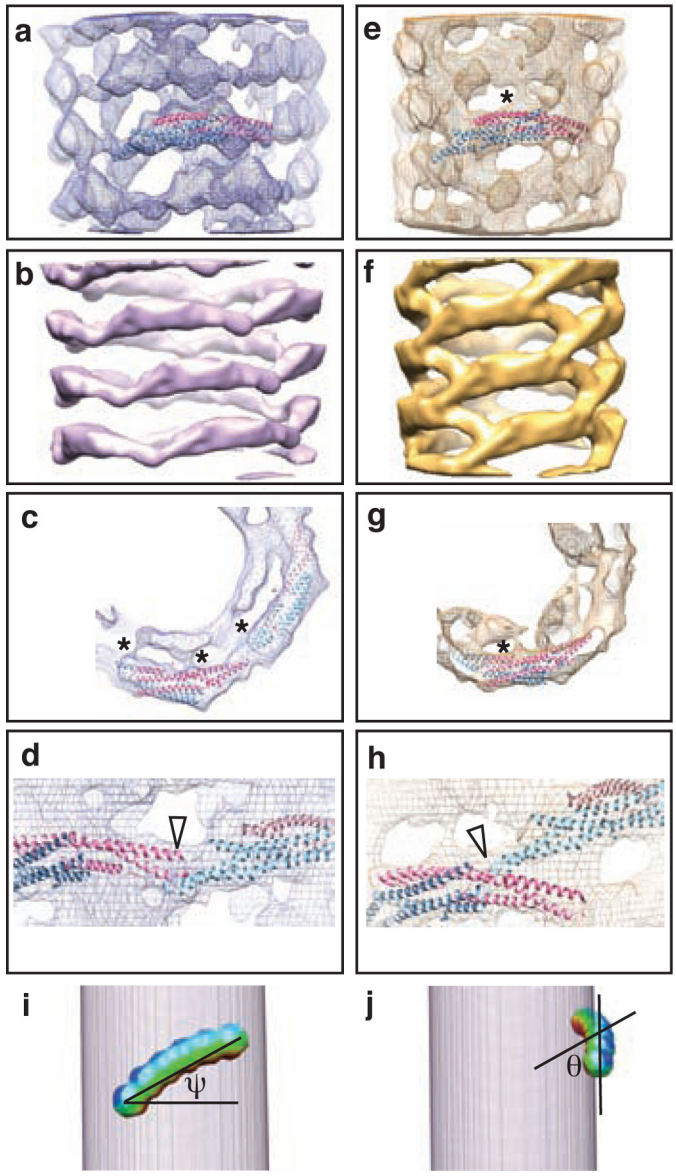

FIGURE 3. Fitting of the endophilin BAR domain structure into cryo-EM reconstructions of the wider (*a–d*) and narrower (*e–h*) tubes. Surface renderings of the reconstructions are shown with *chicken wire representations* in *a*, *c*, *d*, *e*, *h*, and *g*. The fitted atomic models were symmetrized and low pass-filtered at (14 Å)$^{-1}$ in *b* and *f*. *c* and *g*, axial views with two fitted BAR domain dimers in *pink* and *blue*. *Stars* in *c*, *e*, and *g* show the extra densities possibly due to insertion of amphipathic helices. *d* and *h*, two BAR domain dimers magnified and displayed in side view. The wider tube has BAR domain dimers connected tail-to-tail, whereas the narrower tube has some overlaps. The connections between adjacent dimers are indicated with *arrowheads*. *i* and *j*, schematic illustrations defining the tilting angles (γ and φ) of the BAR domains relative to the lipid tube.

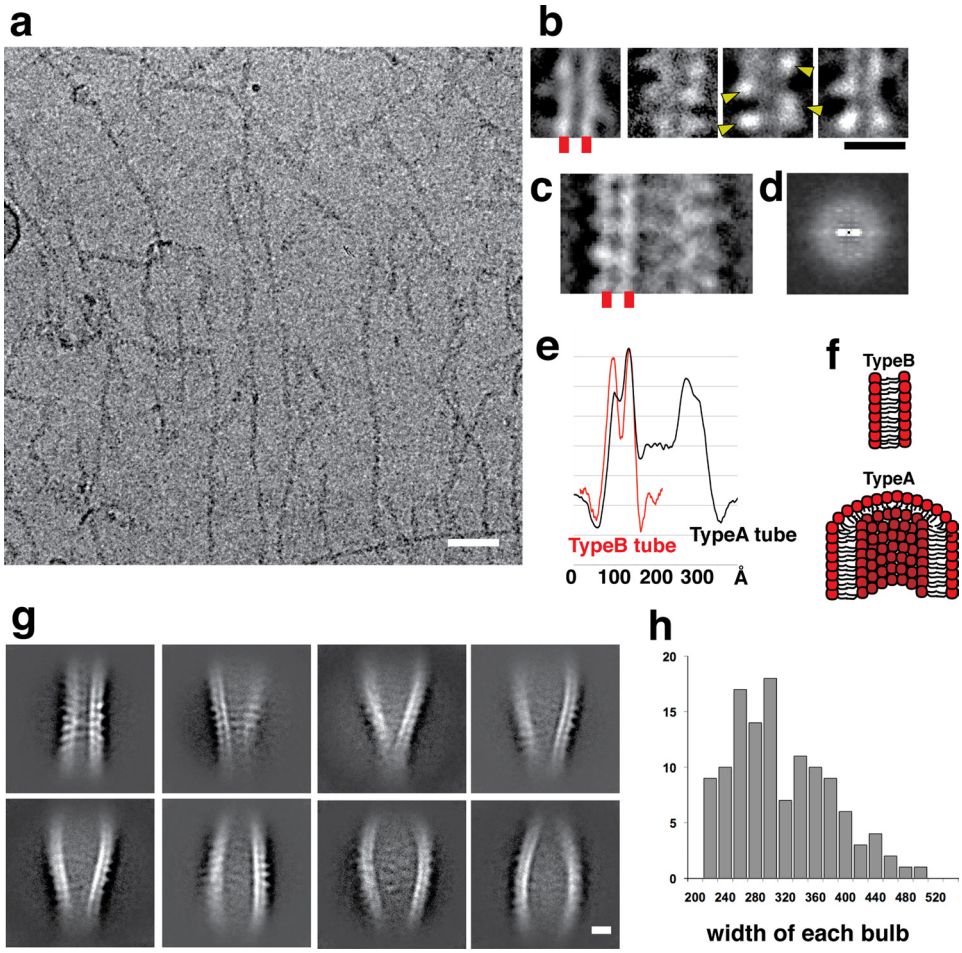

FIGURE 4. *a*, cryoelectron image of Type B tubes. *Scale bar*, 1000 Å. *b*, global average of segments of Type B tubes (*left panel*) and some class averages (*other three panels*). The contrast has been inverted relative to *a*, and high density is light. *Scale bar*, 100 Å. *Yellow arrowheads* point to endophilin-associated densities. *c*, part of a Type A tube, for reference. *Red lines* in *b* and *c* index layers of lipid head groups. *d*, averaged power spectrum of type B tubes. *e*, axial projections of density for Type A tubes in *black* and Type B tubes in *red*. *f*, *schematic illustrations* of lipid configurations in Type B cylindrical micelles and Type A tubes. Endophilins coating the tubes are not shown. *g*, class average images of Type C tubes. *Scale bar*, 100 Å. *h*, distribution of widths of Type C bulbs.

in the wider tubes faces almost perpendicular to the tube axis (Fig. 3*b*, $\theta = 80°$, see Fig. 3*j*), whereas in the narrower tube, it has a slightly inclined arrangement, at $\theta = 52°$. These findings suggest that endophilin BAR domain dimers adapt to the higher curvature of the narrower tube not only by assuming a greater tilt angle but also by rotating around their long axis.

The reconstructions also show densities bridging between the inner and outer leaflets (Fig. 3, *c* and *g*, *asterisks*), as well as densities connecting each BAR domain with its nearest neighbor in the next strands (Fig. 3*e*, *asterisk*). These densities protrude from the BAR domains at points near their tips and their centers, where the amphipathic helices are expected to be located.

At Higher Protein-to-Lipid Ratios, Endophilin Induces Micellar Tube Formation—When the molar ratio of endophilin to lipid was increased to 1:10, we observed Type B tubes, exclusively (Fig. 4*a* and supplemental Fig. 1). These images were also boxed into segments and classified. As these data have lower signal than Type A tubes, we tried different segment lengths in the range of 200–500 Å, seeking to identify features that appear consistently. The main such feature is two parallel lines of density ~35 Å apart (Fig. 4*b*), about the same spacing as between the two leaflets of a coated bilayer on Type A tubes (*cf.* Fig. 4*c*). In some class averages of shorter (~200 Å) segments, we observed isolated peripheral densities (Fig. 4*b*). They are not packed regularly as on Type A tubes but extend out about as far as the serrations on Type A tubes, and we take them also to be endophilin-derived. Adjacent to such densities are the narrowest pieces of tube that we observed which we take to be endophilin-free. We infer from the lack of regularity of these densities that endophilin is not packed regularly on Type B tubes. Consistent with this interpretation, no layer lines were seen in averaged diffraction patterns (*e.g.* Fig. 4*d*).

We interpret the 35-Å peak-to-peak separation of the lines of continuous density to indicate that Type B tubes are coated cylindrical micelles in which the peak densities mark the positions of the lipid head groups (Fig. 4, *e* and *f*). In comparison, spherical phospholipid micelles have a diameter of ~40 Å (32). Also, these thin tubes resemble cylindrical micelles of phosphatidylcholine (33, 34).

The Amphipathic Helices Make Contact with the Tubulated Membranes—The crescent-shaped endophilin dimer is ~130-Å-long (7), whereas the lipid micelles in Type B tubes are only ~45 Å in outer width. Thus, it is possible that the concave surface of the dimer is not fully in contact with the tube. To investigate the folding of the amino acids corresponding to the putative amphipathic helices (H0, H1I), we performed EPR analyses of preparations in which endophilin was spin-labeled with methanethiosulfonate at residues 15 (15R1, H0) and 70 (70R1, H1I). Specimens were prepared at protein-to-lipid ratios of 1:10 (predominantly micellar tubes), 1:20 and 1:40 (predominantly Type A and C tubes (supplemental Fig. 1)). The spectra show changes in the amplitudes of the signals from H0 (Fig. 5, *a* and *c*) and H1I (Fig. 5, *b* and *d*) as soon as endophilin is mixed with lipids, at all protein-to-lipid ratios. This indicates that both motifs become ordered, regardless of tube morphology. The ordering takes place only when they are mixed with lipids. As helices H0 are located near the ends of the BAR dimer, and helices H1I are located near its center, it follows that the entire nether surface of endophilin is in close proximity with the tube. These considerations also suggest that

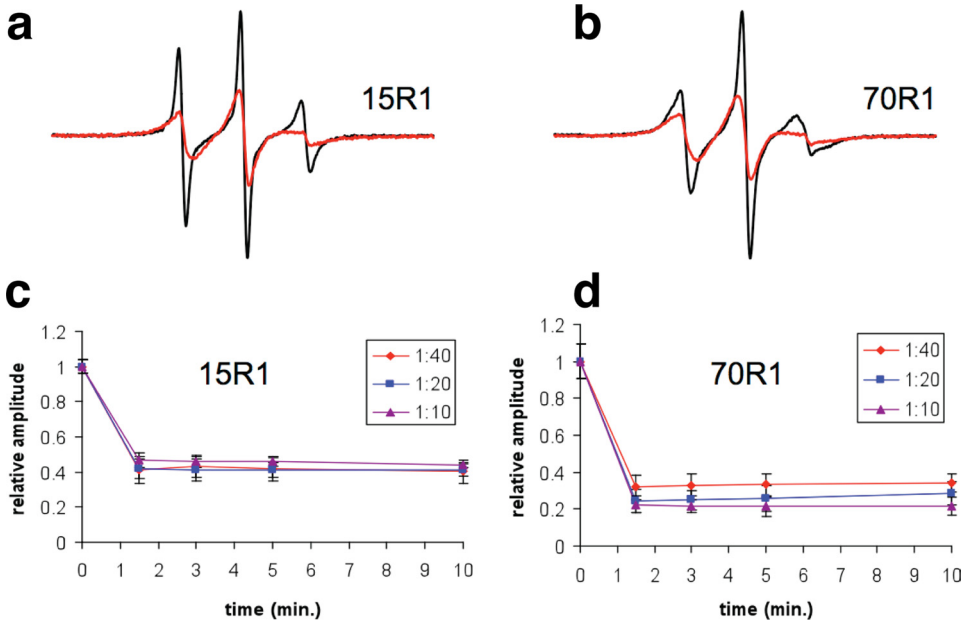

FIGURE 5. **EPR spectral change as a function of time (*a–d*).** EPR spectra are shown in the absence (*black*) and presence of 100% POPG at 1:40 protein-to-lipid molar ratio (*red*) for endophilin 15R1 (*a*) and 70R1 (*b*). Spectra at 1:20 and 1:10 protein-to-lipid molar ratios are similar. Relative EPR spectral amplitude is plotted as a function of incubation time for 15R1 (*c*) and 70R1 (*d*). The decreased EPR spectral amplitude is indicative of ordering. This ordering is due to membrane binding and not simply to decrease in tumbling rate of the protein, as seen in the presence of 30% sucrose (not shown).

the endophilin molecules may be substantially tilted relative to the axis of Type B tubes.

In Type C Tubes, Bulbous Segments Alternate with Narrow Segments—From their observed width, the narrow segments of Type C tubes presumably are micellar, as in Type B tubes (Fig. 1*b*, *arrowhead*). The dimensions of the bulbous segments are fairly regular (Fig. 4*g*), with a maximum width that averages 363 Å (S.D.; 56 Å) (Fig. 4*h*, supplemental Fig. 4*a*) and an average length of 974 Å (S.D.; 176 Å) (supplemental Fig. 4*a*), giving an average radius of curvature of 813 Å (supplemental Fig. 4*b*). As the original vesicles range from 5000 to 20,000 Å in diameter (Fig. 1*f*), there is no correlation between their curvature and that of the bulbous segments. We did not observe any of the wider tubes predicted in molecular dynamic simulations with the N-BAR amphiphysin (21), although these calculations were performed starting with a planar membrane rather than large vesicles.

DISCUSSION

Endophilin Arrays Are Based on Flexible Tail-to-tail Interactions and Lateral Interactions Involving the Amphipathic Helices—We have observed multiple forms of endophilin-induced membrane tubes. Tube morphology correlates with the amount of protein added to induce tubulation, and structural analysis reveals differing arrangements of the coating protein molecules. On Type A tubes, the packing appears to be determined by a combination of tail-to-tail interactions between BAR domain dimers and lateral interactions, probably mediated by the amphipathic helices. At higher endophilin-to-lipid ratios, the membranes are remodeled into cylindrical micelles. We observed no regular packing of endophilin molecules along micellar Type B tubes. However, the change in orientation of the long axis of the endophilin dimer relative to the tube axis between wider and less wide Type A tubes suggests that in Type B tubes, the long axis should be closer to the tube axis. This configuration would enhance the prospect of inserting all or most of the amphipathic helices into the lipid micelle (Fig. 6, *bottom inset*). The overall trend appears to be to maximize contacts of endophilin molecules with lipid head-groups.

We calculate that the narrower Type A tube has a protein-lipid ratio that is ~20% higher than for the wider one: this is mainly because the endophilin dimers pack on a lattice with a smaller unit cell (~ 6,200 Å^2 *versus* ~4,400 Å^2) but also because their cylindrical lipid bilayer has a smaller diameter. While we cannot give a precise figure for the packing density of endophilin on Type B tubes, they should have a still higher protein-to-lipid ratio because micelle lacks an inner leaflet and they are assembled at a higher concentration of added protein. Thus the trend is for coated tubes of lower diameters to have higher protein-to-lipid ratios, and may imply that increasing the local concentration of endophilin squeezes a tubular bilayer into a cylindrical micelle (Fig. 6). On Type C tubes, the bulbous segments have greater diameters than Type A tubes and, by the foregoing argument, we would expect them to have a lower protein-to-lipid ratio. These segments alternate with Type B segments which we take to have the maximum protein-to-lipid ratio. One way to explain this trend would be in terms of some cooperativity in endophilin binding that results in the formation of Type B segments, that depletes the local concentration of endophilin resulting in the intervening bulbous segments; however, if more endophilin is available, no such depletion takes place, and the tubes formed are homogeneously Type B.

Potential Link to Membrane Remodeling in Synaptic Endocytosis—Certain correlations raise the possibility that the endophilin-induced membrane morphologies observed here may relate to membrane remodeling at a synapse. The bulbous segments of Type C tubes average ~360 Å in maximum width, implying that, at least under some circumstances, this curvature is preferentially recognized and stabilized by endophilin. It is similar to that of synaptic vesicles, which are ~420 Å (S.D.; 84 Å) in diameter (35). This correlation suggests that endophilin may be able to sense the curvature of nascent presynaptic endocytic vesicles and bind to them, forming a neck connecting to the plasma membrane. *In situ* cryo-EM studies showed that at the active zone of neuronal termini, (pre)synaptic vesicles are connected by thin densities (see Fig. 7 in Ref. 36). It is not known what these connecting densities are made of nor at which stage of the synaptic vesicle recycling cycle they appear,

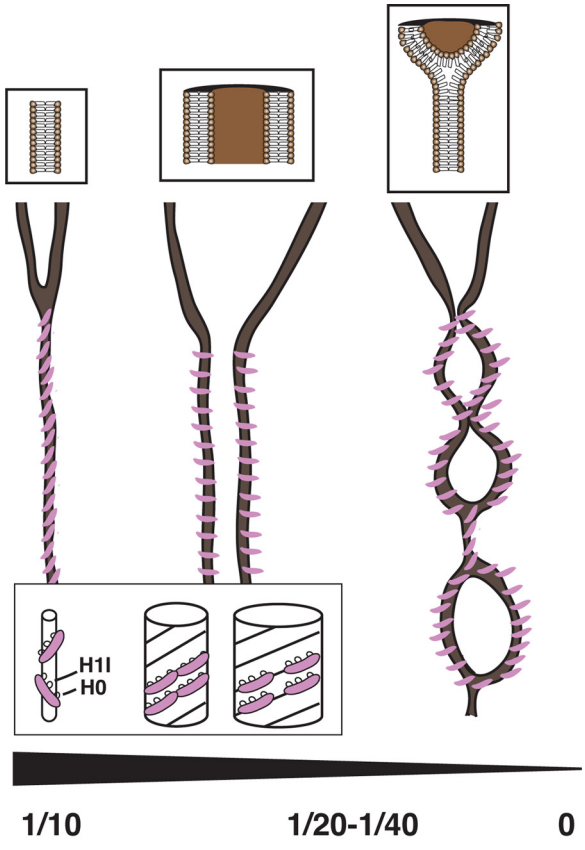

FIGURE 6. **Schematic of various modes of endophilin-induced membrane tubulation.** Depending on the endophilin-to-lipid ratio, the coated tubes assume various morphologies. *Left*, a Type B tube, cylindrical lipid micelles coated with endophilin molecules (*pink lines*) with their long axes predominantly aligned with the tube axis. *Right*, Type C tube with bulbous coated varicosities connected by short Type B-like segments. *Middle*, Type A tube. At the *top* of each segment is shown an uncoated tubular bilayer putatively emanating from a mother vesicle. The ramp at the bottom is for the protein-to-lipid ratio (molar). At the *top*, more detailed diagrams of lipid leaflet topology. *Bottom inset*, schematic illustrations showing how the BAR domains and the amphipathic helices are accommodated on tubes of various diameters.

but the Type C interaction of endophilin is a candidate because it can produce similar morphologies. Thereafter, binding endophilin may increase the curvature of the neck as the invagination pathway progresses, resulting finally in a thin micellar neck (Type B-like; Fig. 6, *left*), the prefinal stage of fission (37–39). In the same vein, a recent study has shown that dynamin squeezes the neck to induce micellar tube formation (hemi-fusion/fission) (40). Because endophilin and dynamin have complementary functions (27, 41–43), it is plausible that they should also share some molecular characteristics. In this scenario, the rates of endophilin binding and subsequent remodeling to reach the hemi-fission state may potentially contribute to the rate control of synaptic cycles. It is noteworthy that a similar relationship may pertain between the remodeling of membrane lipids into a hemi-fusion state and the release of neurotransmitters (39). In conclusion, we acknowledge that our experiments employed a single purified lipid while synaptic vesicles contain several lipids mixed with cholesterol and that although some intriguing correlations have been observed between membrane remodelling *in vitro* and synaptic vesiculation *in vivo*, further experimental information is certainly required.

Acknowledgments—We thank Drs. J. Hinshaw and J. Hurley for constructive advice and helpful discussions and Drs. B Heymann and D. Winkler for support with computational and microscopy resources.

REFERENCES

1. von Gersdorff, H., Vardi, E., Matthews, G., and Sterling, P. (1996) *Neuron* **16,** 1221–1227
2. Rizzoli, S. O., and Betz, W. J. (2005) *Nat. Rev. Neurosci.* **6,** 57–69
3. Takei, K., Slepnev, V. I., Haucke, V., and De Camilli, P. (1999) *Nat. Cell Biol.* **1,** 33–39
4. Frost, A., Unger, V. M., and De Camilli, P. (2009) *Cell* **137,** 191–196
5. Peter, B. J., Kent, H. M., Mills, I. G., Vallis, Y., Butler, P. J., Evans, P. R., and McMahon, H. T. (2004) *Science* **303,** 495–499
6. Wang, Q., Navarro, M. V., Peng, G., Molinelli, E., Goh, S. L., Judson, B. L., Rajashankar, K. R., and Sondermann, H. (2009) *Proc. Natl. Acad. Sci. U.S.A.* **106,** 12700–12705
7. Gallop, J. L., Jao, C. C., Kent, H. M., Butler, P. J., Evans, P. R., Langen, R., and McMahon, H. T. (2006) *EMBO J.* **25,** 2898–2910
8. Tarricone, C., Xiao, B., Justin, N., Walker, P. A., Rittinger, K., Gamblin, S. J., and Smerdon, S. J. (2001) *Nature* **411,** 215–219
9. Henne, W. M., Kent, H. M., Ford, M. G., Hegde, B. G., Daumke, O., Butler, P. J., Mittal, R., Langen, R., Evans, P. R., and McMahon, H. T. (2007) *Structure* **15,** 839–852
10. Shimada, A., Niwa, H., Tsujita, K., Suetsugu, S., Nitta, K., Hanawa-Suetsugu, K., Akasaka, R., Nishino, Y., Toyama, M., Chen, L., Liu, Z. J., Wang, B. C., Yamamoto, M., Terada, T., Miyazawa, A., Tanaka, A., Sugano, S., Shirouzu, M., Nagayama, K., Takenawa, T., and Yokoyama, S. (2007) *Cell* **129,** 761–772
11. Mattila, P. K., Pykäläinen, A., Saarikangas, J., Paavilainen, V. O., Vihinen, H., Jokitalo, E., and Lappalainen, P. (2007) *J. Cell Biol.* **176,** 953–964
12. Masuda, M., Takeda, S., Sone, M., Ohki, T., Mori, H., Kamioka, Y., and Mochizuki, N. (2006) *EMBO J.* **25,** 2889–2897
13. Frost, A., De Camilli, P., and Unger, V. M. (2007) *Structure* **15,** 751–753
14. Itoh, T., Erdmann, K. S., Roux, A., Habermann, B., Werner, H., and De Camilli, P. (2005) *Dev. Cell* **9,** 791–804
15. Saarikangas, J., Zhao, H., Pykäläinen, A., Laurinmäki, P., Mattila, P. K., Kinnunen, P. K., Butcher, S. J., and Lappalainen, P. (2009) *Curr. Biol.* **19,** 95–107
16. Millard, T. H., Bompard, G., Heung, M. Y., Dafforn, T. R., Scott, D. J., Machesky, L. M., and Fütterer, K. (2005) *EMBO J.* **24,** 240–250
17. Arkhipov, A., Yin, Y., and Schulten, K. (2009) *Biophys. J.* **97,** 2727–2735
18. Blood, P. D., and Voth, G. A. (2006) *Proc. Natl. Acad. Sci. U.S.A.* **103,** 15068–15072
19. Arkhipov, A., Yin, Y., and Schulten, K. (2008) *Biophys. J.* **95,** 2806–2821
20. Frost, A., Perera, R., Roux, A., Spasov, K., Destaing, O., Egelman, E. H., De Camilli, P., and Unger, V. M. (2008) *Cell* **132,** 807–817
21. Yin, Y., Arkhipov, A., and Schulten, K. (2009) *Structure* **17,** 882–892
22. Gad, H., Ringstad, N., Löw, P., Kjaerulff, O., Gustafsson, J., Wenk, M., Di Paolo, G., Nemoto, Y., Crun, J., Ellisman, M. H., De Camilli, P., Shupliakov, O., and Brodin, L. (2000) *Neuron* **27,** 301–312
23. Schuske, K. R., Richmond, J. E., Matthies, D. S., Davis, W. S., Runz, S., Rube, D. A., van der Bliek, A. M., and Jorgensen, E. M. (2003) *Neuron* **40,** 749–762
24. Ringstad, N., Gad, H., Löw, P., Di Paolo, G., Brodin, L., Shupliakov, O., and De Camilli, P. (1999) *Neuron* **24,** 143–154
25. Verstreken, P., Kjaerulff, O., Lloyd, T. E., Atkinson, R., Zhou, Y., Meinertzhagen, I. A., and Bellen, H. J. (2002) *Cell* **109,** 101–112
26. Dickman, D. K., Horne, J. A., Meinertzhagen, I. A., and Schwarz, T. L. (2005) *Cell* **123,** 521–533
27. Ringstad, N., Nemoto, Y., and De Camilli, P. (1997) *Proc. Natl. Acad. Sci. U.S.A.* **94,** 8569–8574
28. Weissenhorn, W. (2005) *J. Mol. Biol.* **351,** 653–661

29. Cui, H., Ayton, G. S., and Voth, G. A. (2009) *Biophys. J.* **97,** 2746–2753
30. Bhatia, V. K., Madsen, K. L., Bolinger, P. Y., Kunding, A., Hedegård, P., Gether, U., and Stamou, D. (2009) *EMBO J.* **28,** 3303–3314
31. Egelman, E. H. (2000) *Ultramicroscopy* **85,** 225–234
32. Chou, J. J., Baber, J. L., and Bax, A. (2004) *J. Biomol. NMR* **29,** 299–308
33. Walter, A., Vinson, P. K., Kaplun, A., and Talmon, Y. (1991) *Biophys. J.* **60,** 1315–1325
34. Vinson, P. K., Talmon, Y., and Walter, A. (1989) *Biophys. J.* **56,** 669–681
35. Takamori, S., Holt, M., Stenius, K., Lemke, E. A., Gronborg, M., Riedel, D., Urlaub, H., Schenck, S., Brügger, B., Ringler, P., Müller, S. A., Rammner, B., Gräter, F., Hub, J. S., De, Groot, B. L., Mieskes, G., Moriyama, Y., Klingauf, J., Grubmüller, H., Heuser, J., Wieland, F., and Jahn, R. (2006) *Cell* **127,** 831–846
36. Fernández-Busnadiego, R., Zuber, B., Maurer, U. E., Cyrklaff, M., Baumeister, W., and Lucic, V. (2010) *J. Cell Biol.* **188,** 145–156
37. Chernomordik, L. V., and Kozlov, M. M. (2008) *Nat. Struct. Mol. Biol.* **15,** 675–683
38. Jahn, R., Lang, T., and Südhof, T. C. (2003) *Cell* **112,** 519–533
39. Rigoni, M., Caccin, P., Gschmeissner, S., Koster, G., Postle, A. D., Rossetto, O., Schiavo, G., and Montecucco, C. (2005) *Science* **310,** 1678–1680
40. Bashkirov, P. V., Akimov, S. A., Evseev, A. I., Schmid, S. L., Zimmerberg, J., and Frolov, V. A. (2008) *Cell* **135,** 1276–1286
41. De Camilli, P., Takei, K., and McPherson, P. S. (1995) *Curr. Opin. Neurobiol.* **5,** 559–565
42. Farsad, K., Ringstad, N., Takei, K., Floyd, S. R., Rose, K., and De Camilli, P. (2001) *J. Cell Biol.* **155,** 193–200
43. Anggono, V., and Robinson, P. J. (2007) *J. Neurochem.* **102,** 931–943
44. Heymann, J. B., and Belnap, D. M. (2007) *J. Struct. Biol.* **157,** 3–18
45. Ludtke, S. J., Baldwin, P. R., and Chiu, W. (1999) *J. Struct. Biol.* **128,** 82–97
46. Shaikh, T. R., Gao, H., Baxter, W. T., Asturias, F. J., Boisset, N., Leith, A., and Frank, J. (2008) *Nat. Protoc.* **3,** 1941–1974
47. Pettersen, E. F., Goddard, T. D., Huang, C. C., Couch, G. S., Greenblatt, D. M., Meng, E. C., and Ferrin, T. E. (2004) *J. Comput. Chem.* **13,** 1605–1612
48. Mears, J. A., and Hinshaw, J. E. (2008) *Meth. Cell Biol.* **88,** 237–256
49. Jao, C. C., Hegde, B. G., Gallop, J. L., Hegde, P. B., McMahon, H. T., Haworth, I. S., and Langen, R. (2010) *J. Biol. Chem.* **285,** 20164–20170